energies

MDPI

Article

Large Eddy Simulation of Rotationally Induced Ingress and Egress around an Axial Seal between Rotor and Stator Disks

Sabina Nketia [1], Tom I-P. Shih [1,*], Kenneth Bryden [2], Richard Dalton [3] and Richard A. Dennis [3]

[1] School of Aeronautics and Astronautics, Purdue University, West Lafayette, IN 47907, USA; snketia@purdue.edu
[2] Ames National Laboratory, U.S. Department of Energy, Ames, IA 50011, USA; kmbryden@iastate.edu
[3] National Energy Technology Laboratory, U.S. Department of Energy, Morgantown, WV 26505, USA; richard.dalton@netl.doe.gov (R.D.); richarddennis578@gmail.com (R.A.D.)
* Correspondence: tomshih@purdue.edu

Abstract: In gas turbines, the hot gas exiting the combustor can have temperatures as high as 2000 °C, and some of this hot gas enter into the space between the stator and rotor disks (wheelspace). Since the entering hot gas could damage the disks, its ingestion must be minimized. This is carried out by rim seals and by introducing a cooler flow from the compressor (sealing flow) into the wheelspace. Ingress and egress into rim seals are driven by the stator vanes, the rotor and its rotation, and the rotor blades. This study focuses on the ingress and egress driven by the rotor and its rotation. This is carried out by performing wall-resolved large eddy simulation (LES) around an axial seal in a rotor–stator configuration without vanes and blades. Results obtained show the mechanisms by which the rotor and its rotation induce ingress, egress, and flow trajectories. Kelvin–Helmholtz instability was found to create a wavy shear layer and displacement thickness that produces alternating regions of high and low pressures around the rotor side of the seal. Vortex shedding on the backward-facing side of the seal and its impingement on the rotor side of the seal also produces alternating regions of high and low pressures. The locations of the alternating regions of high and low pressures were found to be statistically stationary and to cause ingress to start on the rotor side of the seal. Vortex shedding and recirculating flow in the seal clearance also cause ingress by entrainment. With the effects of the rotor and its rotation on ingress and egress isolated, this study enables the effects of stator vanes and rotor blades to be assessed.

Keywords: gas turbines; rim seals; rotationally induced ingress

Citation: Nketia, S.; Shih, T.I.-P.; Bryden, K.; Dalton, R.; Dennis, R.A. Large Eddy Simulation of Rotationally Induced Ingress and Egress around an Axial Seal between Rotor and Stator Disks. *Energies* **2023**, *16*, 4354. https://doi.org/10.3390/en16114354

Academic Editor: Rob J.M. Bastiaans

Received: 17 April 2023
Revised: 20 May 2023
Accepted: 23 May 2023
Published: 26 May 2023

1. Introduction

The efficiency of gas turbine engines increases as the temperature of the gas entering the turbine component increases. In advanced gas turbines, those temperatures far exceed the melting temperature of the turbine material [1,2]. Thus, all parts of the turbine that come in contact with the hot gas must be cooled. In addition, some of the hot gas could enter into the space between the stator disk and the rotor disk (referred to as the wheelspace).

The ingestion of hot gas into the wheelspace (referred to as ingress) must be minimized or prevented. This is because the Ni-based superalloy used to make the disks can only handle temperatures up to about 850 °C [3]. Ingress is minimized by rim seals and by introducing a cooler flow known as sealing flow into the wheelspace. Since the sealing flow is extracted from the compressor, air that could be used to generate power, the amount of sealing flow used must be minimized. Currently, 15 to 20% of the air entering the high-pressure compressor (HPC) is used to cool the turbine, where the sealing flow accounts for up to 10% of that total cooling flow [4].

Preventing or minimizing hot gas ingestion requires in-depth understanding on how geometry and rotation affect fluid flow that leads to hot gas ingestion. Ingress and egress through the rim seal are driven by (1) the rotor disk and its rotation, (2) the pressure variation around the stator vanes' trailing edges, and (3) stagnation pressure induced by the rotor blades. This study focuses on ingress induced by the rotor disk and its rotation (referred to as rotationally induced ingress), which has received less attention.

Owen and co-workers experimentally studied the effectiveness of axial, radial, and mitered seals on ingress induced by rotation in a configuration without vanes and blades [5–9] and in a configuration with vanes and blades [10]. For an axial seal, Owen and Phadke [5] showed that if the gap ratio ($G = s/r_o$) is fixed, then the minimum sealing flow necessary to prevent ingress, $C_{W,min}$, is $C_{W,min} = 0.14 G_c^{0.66} Re_\phi$, where $G_c = s_c/r_o$ is the clearance ratio and $Re_\phi = \rho_h \omega r_o^2/\mu_h$ is the rotational Reynolds number. For radial seals, Phadke and Owen [6] showed that they provide more effective sealing than the axial seals because radial seals enable higher pressures in the wheelspace. In the study by Phadke and Owen [7], the minimum sealing flow necessary for the axial, radial, and mitered seals to prevent ingress, $C_{W,min}$, was found to be directly proportional to the rotational speed and the sealing clearance. When there is flow in the hot gas path, Phadke and Owen [8] showed that when $0.60 < Re_w/10^6 < 1.7$, where $Re_w = \rho_h V_h r_o/\mu_h$ is the Reynolds number in the hot gas path, the effectiveness of axial and radial seals are comparable. Additionally, for $0 < Re_w/10^6 < 0.5$, $C_{W,min}$ was found to be independent of rotational speeds if $Re_w/Re_\phi = V_h/(\omega r_o) \gg 1$ (externally dominated regime or $V_h \gg \omega r_o$) and directly proportional to rotational speeds if $Re_w/Re_\phi = V_h/(\omega r_o) \ll 1$ (rotationally dominated regime or $V_h \ll \omega r_o$). In the externally dominated regime, the most important factor affecting ingress is the size of the seal clearance. In the rotationally dominated regime, the flow in the hot gas path reduces $C_{W,min}$ to about half of the value required for zero external flow. When the flow in the hot gas path is not axisymmetric, Phadke and Owen [9] showed that $C_{W,min}$ increases with increasing pressure asymmetries. Phadke and Owen [9] also studied the double-shrouded seal and found it to be more effective than the axial and radial seals. This is because with two shrouds, the ingested fluid is trapped between them so that less enter into the wheelspace. Sangan et al. [10] showed the sealing flow needed to prevent rotationally induced ingress is lower than that needed to prevent externally induced ingress and that for rotationally induced ingress, the maximum flow that can be ingested is 35% of the flow required to seal the system. Dadkhah et al. [11] experimentally studied a radial seal and showed the effects of the seal location in a two-stage turbine. Bohn et al. [12] also experimentally studied ingress in a rotor–stator configuration without vanes and blades and showed hot gas ingestion to occur not only on the stator side but also on the rotor side of the seal.

Computational studies of ingress have also been performed [13–18]. Cao et al. [13] studied how sealing flow interacts with the hot gas flow in the annulus. Boudet et al. [14] studied the same configuration as Cao et al. [15] and observed nonlinear coupling among the flow features. Jakoby et al. [16] showed a large-scale structure forming in the wheelspace and how it strongly influences ingestion. Rabs et al. [16] observed Kelvin–Helmholtz instabilities around the rim seal in a 1.5-stage turbine and attributed their formation to swirl introduced upstream of the seal. They also observed regions of high and low pressure in the circumferential direction around the seal and hypothesized the Kelvin–Helmholtz vortices as the cause. Gao et al. [17] found LES to correctly predict the peak frequency but not the number of structures when compared with experiments. Liu et al. [18] showed that if steady RANS is used to study ingress, where an inertial frame is used for the stator and a noninertial frame is used for the rotor, then the location of the interface between the inertial and the noninertial frames must be located downstream of the rim seal but upstream of the rotor.

This review of the literature shows theoretical, computational, and experimental approaches have been applied to study rotationally induced ingress. These studies have focused on effects of variables such as flow rate and rotor speed on ingress and flow features. However, details of the flow in the seal and wheelspace as well as the physical mechanisms that give rise to these flow features are still not well understood. The objective of this study is to use steady RANS (Reynolds-averaged Navier–Stokes) and wall-resolved large eddy simulation (LES) to examine the details of the turbulent flow and trajectories of ingress in a rotor–stator configuration with an axial seal and without vanes and blades. The intent is to isolate the effects of the rotor and its rotation on ingress and egress and understand how ingress and sealing flow could be minimized under conditions where rotationally-induced ingress is the dominant mechanism. Also, once flow mechanisms induced by the rotor and its rotation are isolated, one can better understand mechanisms induced by stator vanes and rotor blades.

The remainder of this paper is organized as follows: First, the rotor–stator problem studied is described. Next, the governing equations and numerical methods used are summarized. Afterwards, a grid-sensitivity and validation study are presented. This is then followed by the results obtained for the flow around the seal. Finally, the key conclusions are summarized.

2. Problem Description

A schematic of the stator–rotor configuration studied is shown in Figure 1. The hot gas path is an annulus with inner radius r_o = 116.25 mm and outer radius r_1 = 165.25 mm. The stator disk extends from $z = -(L_1 + L_d + s_c)$ to $z = -s_c$, and the rotor disk extends from $z = 0$ to $z = L_2 - (L_1 + L_d + s_c)$, where L_1 = 150 mm, L_2 = 210.7 mm, L_d = 10 mm, and s_c = 1.7 mm. An axial seal is located between $z = -s_c$ and $z = 0$, and it has a thickness of d_c = 4.5 mm. The distance between the stator and rotor disks is s = 16.7 mm. An extension section of length L_3 = h was appended to the rotor to ensure no reverse flow at the outflow boundary. For this extended section, the walls were adiabatic and allowed to slip so that no heat or friction are added. Sealing flow is fed from an annular duct of length L_4 = 20 mm with inner radius r_2 = 10 mm and outer radius r_3 = 12 mm. For this annular duct, the inner wall was modeled as adiabatic and allowed to slip.

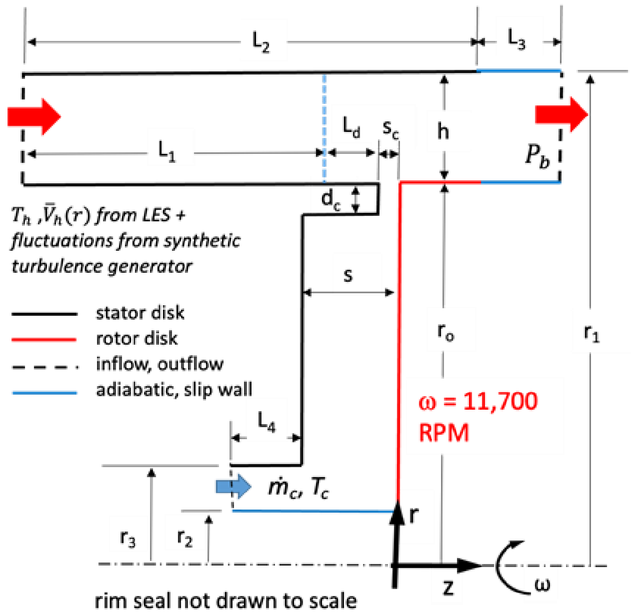

Figure 1. Schematic of the rotor–stator configuration studied (r_o = 116.25 mm, r_1 = 165.25 mm, s_c = 1.7 mm, d_c = 4.5 mm, L_1 = 150 mm, L_2 = 210.7 mm, L_3 = h, L_4 = 20 mm, L_d = 10 mm, and $h = r_1 - r_o$).

For this rotor–stator configuration with an axial seal, the gas that enters the hot gas path is air with zero swirl. Its mass flow rate and temperature are $\dot{m}_h$ = 3.42 kg/s and $T_h = 333\ K$, amounting to $Re_w = 0.46 \times 10^6$. The pressure at the exit of the hot gas path is P_b = 101,325 Pa. The sealing flow that enters has a mass flow rate of $\dot{m}_c = 0.002089$ kg/s and a temperature of $T_c = 290$ K, amounting to $C_W = 1000$. Simulations were also performed with zero sealing flow, where the entrance was made into an adiabatic slip wall to examine the worst-case scenario. The rotor rotates at a constant angular velocity of ω = 11,700 RPM, amounting to $Re_{\phi} = 1.13 \times 10^6$. All surfaces in black (stator and outer radius of annulus) and red (rotor) are no-slip and adiabatic. Surfaces in blue (extension section and part of the sealing flow feed duct) are slip and adiabatic.

This configuration was selected because it matches an experimental study by Bohn et al. [12], where there are experimental data that are used to validate this study. Additionally, the selected problem helps us to meet the objectives of this study.

3. Problem Formulation

The problem described in the previous section were computed by using steady RANS and LES. For RANS, the governing equations used are the ensemble-averaged continuity, Navier–Stokes, and energy equations for a thermally and calorically perfect gas. Effects of turbulence were modeled by the shear stress transport (SST) model [19]. The boundary conditions used are as follows: At the inlet of the hot gas path, velocity (a "fully-developed" profile based on incompressible flow with zero swirl) and temperature (a uniform profile) were specified. At the outlet of the hot gas path, pressure was specified. At all solid surfaces except those marked in blue in Figure 1, the no-slip, adiabatic wall boundary conditions were imposed. At solid surfaces marked in blue, the slip, adiabatic wall boundary conditions were imposed.

For LES, the governing equations used are the spatially filtered continuity, Navier–Stokes, and energy for an ideal gas. With LES, the large scales of the turbulent flow are resolved, and the smaller scales are modelled in terms of the resolved larger scales via the subgrid-scale stresses, τ_{ij}, where

$$\widetilde{\tau}_{ij} = -2\nu_{sgs}\hat{S}_{ij} + \frac{1}{3}\widetilde{\tau}_{kk}\delta_{ij}$$

In this study, the WALE model [20] was employed to model the sub-grid scale turbulent viscosity, ν_{sgs}, and it is given by

$$\nu_{sgs} = (C_{LES}\Delta)^2 \frac{\left(S^d_{ij}S^d_{ij}\right)^{\frac{3}{2}}}{\left(\hat{S}_{ij}\hat{S}_{ij}\right)^{\frac{5}{2}} - \left(S^d_{ij}S^d_{ij}\right)^{\frac{5}{4}}}$$

where $C_{LES} = 0.325$ is a model constant; Δ is the cutoff width (grid spacing was used); and

$$S^d_{ij} = \hat{S}_{ik}\hat{S}_{kj} + \hat{\Omega}_{ik}\hat{\Omega}_{kj} - \frac{1}{3}\left(\hat{S}_{mn}\hat{S}_{mn} - \hat{\Omega}_{mn}\hat{\Omega}_{mn}\right)\delta_{ij}$$

Since the WALE model produces proper scaling (namely, $\upsilon_{sgs} \sim y^3$) near the wall, damping functions are not needed. Additionally, this model is sensitive to both the strain ($\hat{S}_{ij}$) and the rotation rate ($\hat{\Omega}_{ij}$) of the resolved smaller structures.

Synthetic turbulence [21] with 3% turbulence intensity was used to trigger the turbulence at the inlet of the hot gas path. L_1 = 150 mm was the "adaptation distance" obtained by numerical experiments to ensure that the profiles of the velocity and the turbulent characteristics match that of the "fully-developed" turbulent flow at a distance of L_d upstream of the rim seal. This adaptation distance is peculiar to this case without vanes and without blades, and with the quoted hot gas mass flow rate in the description of the problem. When these parameters change, a new adaptation distance had to be re-calculated. The other boundary conditions are the same as those used for RANS. The results from the RANS simulation were used as the initial conditions for the LES.

To reduce computational cost, only a 10-degree sector of the rotor–stator configuration was studied for both RANS and LES, where periodic conditions were imposed at the two r–z planes that bound the sector. The sector size selected is assessed in the section on verification.

4. Numerical Method of Solution

Solutions to RANS and LES were obtained by using Version 22.1 of the Fluent ANSYS code [22]. For steady RANS, the advection terms were approximated by second-order upwind differencing, and diffusion terms were approximated by second-order central differencing. Solutions were generated by using the coupled scheme At convergence, the "scaled" residuals plateaued and were less than 10^{-6} for continuity, less than 10^{-8} for the three components of the velocity, and less than 10^{-10} for energy. For LES, the bounded second-order implicit scheme was used for the time derivative, and the second-order central was used for all advection and diffusion terms. The pressure staggering option (PRESTO) scheme was used for pressure interpolation at cell faces from cell centers. The SIMPLE scheme [23] was used as the solver. Since time-accurate solutions were of interest, iterations were performed at each time step until the residuals plateaued. This required 40 to 50 iterations per time step. At convergence, the "scaled" residuals were less than 10^{-6} for continuity, less than 10^{-7} for the three components of the velocity, and less than 10^{-8} for energy. For the LES, each simulation was run until statistically stationary solutions were obtained, which took 11 revolutions for the problem studied. Once statistically stationary, the LES solution was time-averaged to obtain the mean flow, which required from two to five revolutions. At this point, it is noted that the solution is time-periodic. However, only the statistically stationary results are presented.

5. Results and Discussion

In this section, the results from the verification and validation studies are first presented. Next, the computed flow field around the axial seal is described. This is followed by a discussion on the flow mechanisms that created the flow field and how ingress and egress occur.

5.1. Verification and Validation

The verification and validation of this study were accomplished by simulating two problems. One is the fully developed incompressible turbulent flow in an annulus, where there are detailed experimental and direct numerical simulation data available in the literature that can be used to guide the grid-resolution needed to obtain the correct physics and to validate the solutions from LES. The other problem is the stator–rotor configuration shown in Figure 1, where there are data on the mean flow velocities for validation.

5.1.1. Fully Developed Flow in an Annulus

Figure 2 shows the annular duct studied (not drawn to scale). It has an inner radius of r_o = 10.05 mm, an outer radius of r_1 = 20.15 mm, and a length of L_5 = 6.4 h, where $h = r_1 - r_o$. The mass flow rate in the annulus is $\dot{m}$ = 0.02523 kg/s, where the density is taken to be a constant at temperature T = 333 K and pressure P = 1 atm so that the average mean speed is U_b = 24.8 m/s. The resulting Reynolds number is Re_{Dh} = 26,600. These geometric and operating parameters were selected to match those employed in the experimental study by Nouri et al. [24] and the DNS study by Quadrio and Luchini [25].

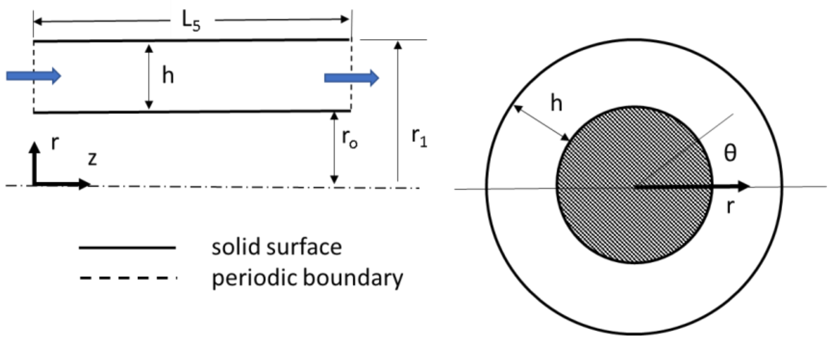

Figure 2. Schematic of annulus studied (r_o = 10.05 mm, r_1 = 20.15 mm, h = 10.1 mm, L_5 = 6.4 h).

The governing equations and method of solution method are identical to those described in the previous sections, except that the governing equations are for incompressible flow with constant viscosity so that the continuity and momentum equations are decoupled from the energy equation. For the LES, it took 20 flow-throughs to obtain statistically stationary solutions and another 10 flow-throughs to achieve the time-averaged results.

The fully developed velocity in the annular duct was obtained by imposing periodic boundary condition in the streamwise direction, where the mean pressure is adjusted to achieve the desired mass flow rate and where the initial turbulent fluctuations for the LES were generated by synthetic turbulence.

Concerning the length of the annular duct, L_5, it was set long enough to ensure that turbulence at the inlet and the outlet, the two periodic boundaries, is not correlated. According to Kim et al. [26], that length should be 6.4 D_h, where D_h is the hydraulic diameter. In this study, L_5 = 6.4 h = 3.2 D_h was found to be adequate based on the longitudinal two-point correlation. To reduce computational cost, only an angular sector of the annular duct was simulated, invoking periodicity in the azimuthal direction. According to Quadrio and Luchini [25], the minimum angular sector needed for LES depends on the curvature parameter, $\gamma = \frac{r_1 - r_o}{2r_o}$. If $\gamma < 1$, then the effects of curvature can be neglected [25]. For the annular duct studied, $\gamma \approx 0.5$, which is less than unity. Thus, the sector size only needs to meet the requirements of LES for planar channel flows. For planar channel flows, Kim et al. [26] recommended a spanwise dimension of $\approx 3.2(r_1 - r_o)$, which is equal to an angle of $\Delta\theta \approx 90^\circ$ for the annular duct. In this study, a sector of $\Delta\theta = 120^\circ$ was used.

Figure 3 shows the three grids used in the grid-sensitivity study: a coarse grid with 61 × 73 × 101 nodes, a baseline grid with 81 × 145 × 201 nodes, and a fine grid with 95 × 181 × 281 nodes. For all three grids, the first cells next to the walls are clustered such that y^+ is less than unity. Additionally, there are at least five cells within y^+ = 5. The nondimensional grid spacings are $\Delta r^+ < 20$, $\Delta z^+ < 20$, and $r\Delta\theta^+ < 20$ for the coarse grid, $\Delta r^+ < 10$, $\Delta z^+ < 10$, and $r\Delta\theta^+ < 10$ for the baseline grid, and $\Delta r^+ < 7$, $\Delta z^+ < 7$, and $r\Delta\theta^+ < 7$ for the fine grid.

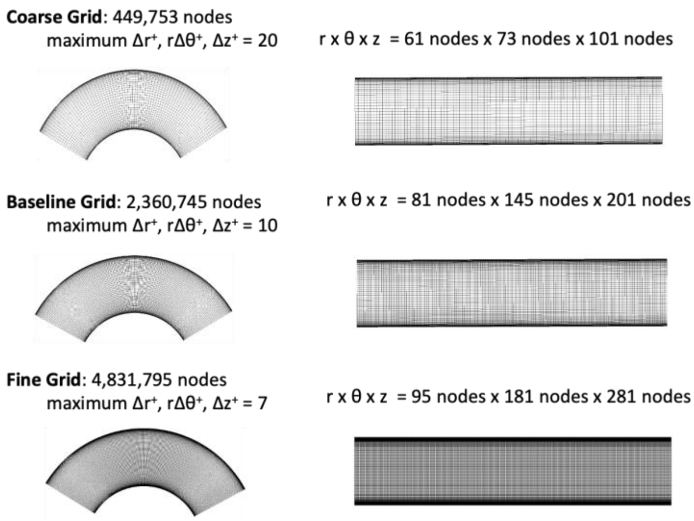

Figure 3. Grids used for annular duct.

Concerning the time step size, the DNS study of Quadrio and Luchini [25] suggests a time step size of $\Delta t \approx 4.1 \times 10^{-6}$ s for this problem. In this study, two time step sizes were examined, $\Delta t = 10^{-5}$ s and $\Delta t = 10^{-6}$ s, and $\Delta t = 10^{-6}$ s was used for all simulation results presented.

The results obtained by using the three grids with $\Delta t = 10^{-6}$ s are shown in Figures 4 and 5. The results for the mean velocity and root mean square of velocity fluctuations obtained with the baseline grid are in good agreement with the DNS from Quadrio and Luchini [25] with $\gamma = 1$.

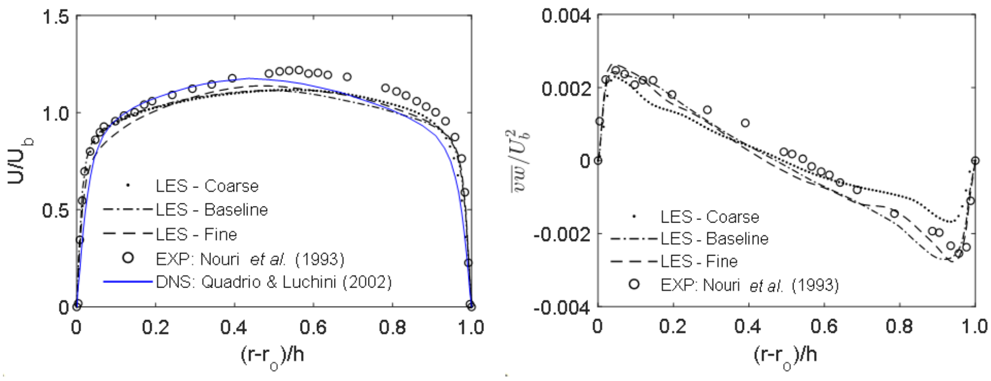

Figure 4. Mean axial velocity and axial-radial velocity correlation in the annular duct obtained by the three grids [24,25].

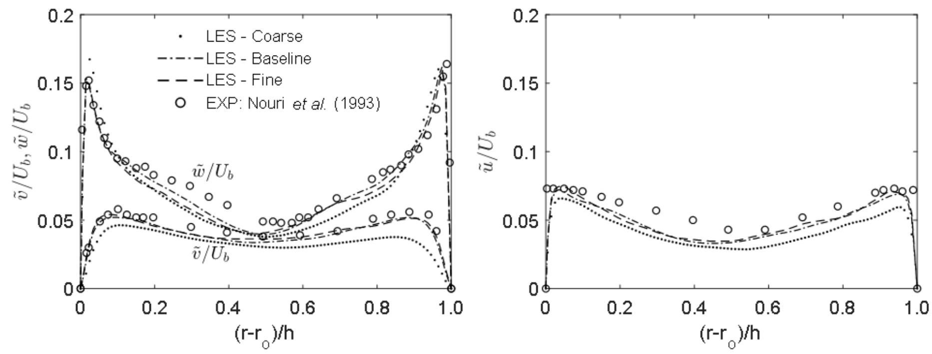

Figure 5. Root mean square of the velocity fluctuations in the annular duct obtained by the three grids [24].

With $\Delta t = 10^{-6}$ s, all three grids were inspected to see if they satisfy the Celik criterion [27], which states that the LES_IQ must be greater than 0.8. In Figure 6, it can be seen that the LES_IQ values for all the three grids are greater than 0.9 everywhere in the annular duct, which is greater than the required level of 0.8. This shows that 90+% of the turbulent kinetic energy in the flow is resolved by the LES.

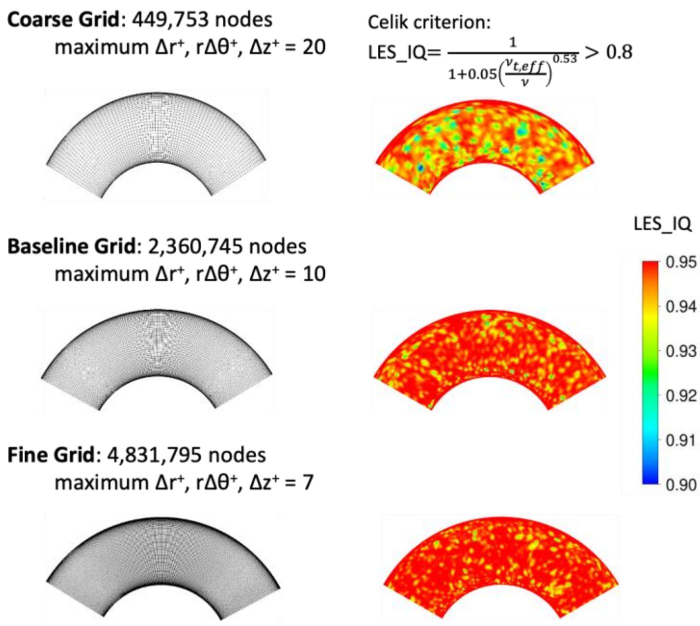

Figure 6. LES_IQ for all three grids in the annular duct.

Figure 7 shows the energy spectra from the axial velocities at three probe locations in the annular duct obtained using the baseline grid: r = r_o + 0.05, (r_o + r_1)/2, r_1 − 0.05, z = 3.2 h, and θ = 60°. From this figure, the energy spectra can be seen to follow Kolmogorov's −5/3 law for a range of frequencies before falling. The energy densities associated with high frequencies are at least seven orders lower than the energy densities corresponding to low frequencies in the inertial sub-range. Thus, the grid resolution of the baseline grid is adequate.

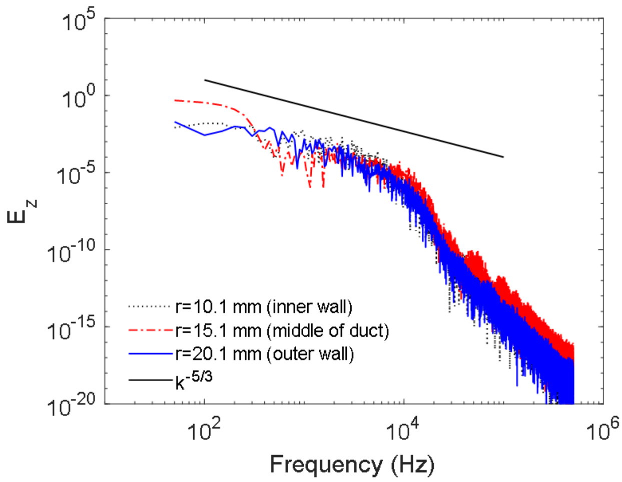

Figure 7. Energy spectra from the axial velocity at three probe locations in the annular duct. The $k^{-5/3}$ line is to show the slope.

Figure 8 shows the two−point correlation along a line in the middle of the annulus from the annular duct's inlet to its exit with one probe at the inlet. From this figure, it can be seen that the two-point correlation acquired from the second probe falls off to zero at less than half of the duct length. Thus, the length, $L_5 = 6.4(r_1 - r_o)$ is sufficient to implement periodic boundary conditions for the incompressible fully developed flow in the annular duct.

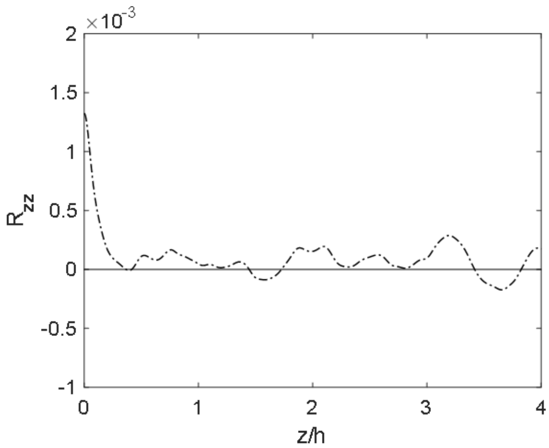

Figure 8. Two-point correlation along a line in the middle of the annulus from annular duct's inlet to exit.

5.1.2. Rotor–Stator Configuration with Axial Seal

The problem description, formulation, and method of solution for the rotor–stator configuration were already described in previous sections. Concerning the size of the computational domain in the azimuthal direction, the angle of the sector must be sufficiently large to resolve the relevant flow physics. RANS was used to run three sector sizes—10°, 20°, and 30°—to examine the nature of the flow in the azimuthal direction. Figure 9 shows the pressure distribution on the surface of the hot gas path located at r = r_o. From this figure, variations in the azimuthal direction can be seen, and the wavelength of those variations are much smaller than the arc length intercepted by a sector of 10 degrees. Additionally, the wavelength of the variations is independent of the sector size. Thus, the 10-degree sector is sufficient for this study based on RANS.

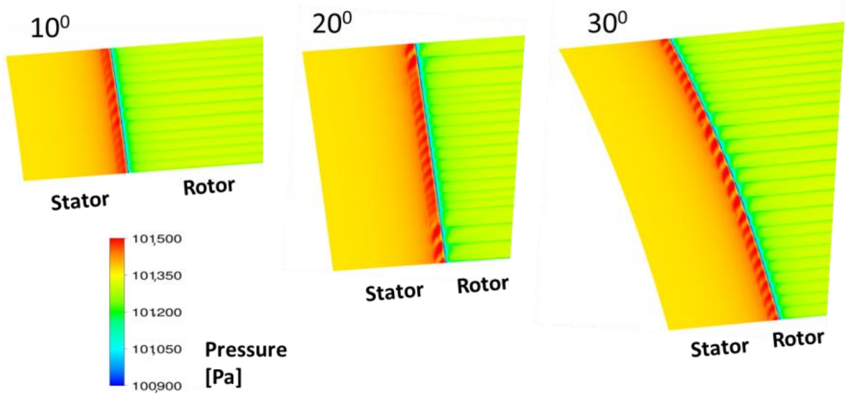

Figure 9. Pressure on hot gas surface located at r = r_o for different sector sizes obtained by RANS.

Though the 10-degree sector may be adequate for RANS, for LES, the azimuthal velocities at the two periodic boundaries in the azimuthal direction must be uncorrelated. Thus, a simulation was performed with LES to ensure that this is indeed the case. Figure 10 shows that the azimuthal two−point correlation is indeed uncorrelated if the sector size is 10 degrees (even for Point A).

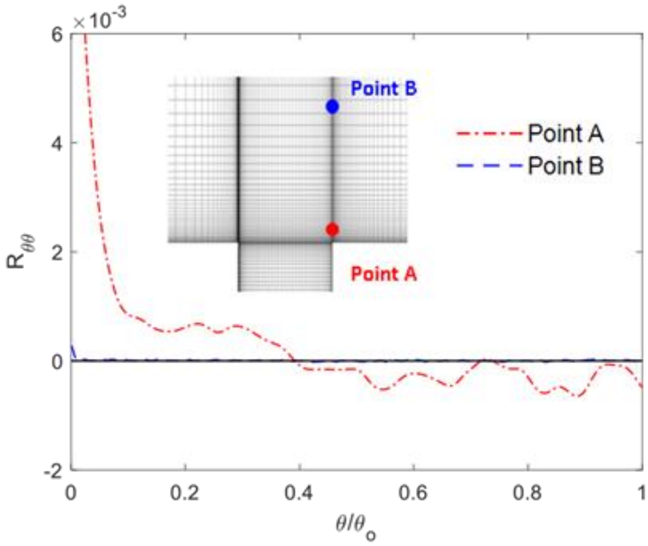

Figure 10. Azimuthal two−point correlation for Point A and Point B along the azimuthal direction from θ/θ_o = 0 to 1 around the axial seal.

Figure 11 shows the three grids used in the grid-sensitivity study: a coarse grid, a baseline grid, and a fine grid. The number of grid points across the seal clearance is 41 for the coarse grid, 61 for the baseline grid, and 81 for the fine grid. The number of grid points across the 10° sector in the azimuthal direction is 101 for the coarse and baseline grids and 201 for the fine grid. For all grids, the first cells next to the walls are clustered such that y^+ is less than unity (see Figure 12). Additionally, there are at least five cells within $y^+ = 5$. Away from the seal, the nondimensional grid spacings satisfy $\Delta r^+ < 30$, $\Delta z^+ < 30$, and $r\Delta\theta^+ < 30$ for the coarse grid, $\Delta r^+ < 20$, $\Delta z^+ < 20$ and $r\Delta\theta^+ < 20$ for the baseline grid, and $\Delta r^+ < 10$,

$\Delta z^+ < 10$ and $r\Delta\theta^+ < 10$ for the fine grid. In the seal region, the highest friction velocity was used to compute the nondimensional spacings.

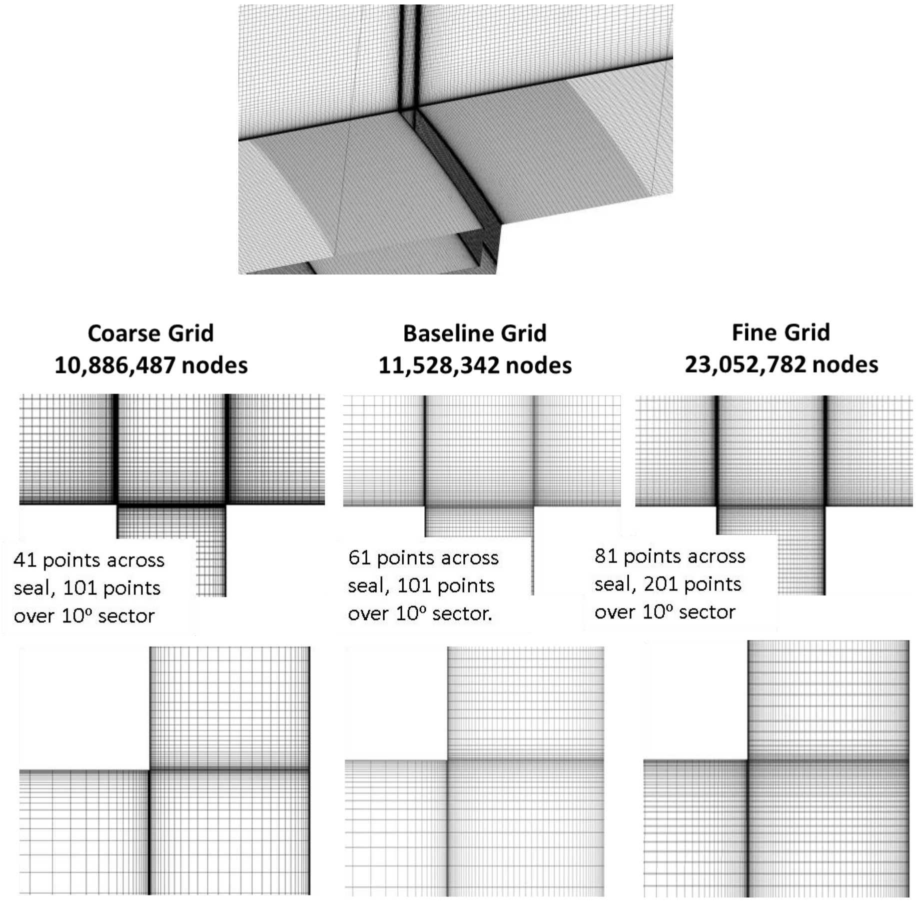

Figure 11. Grids used around the seal.

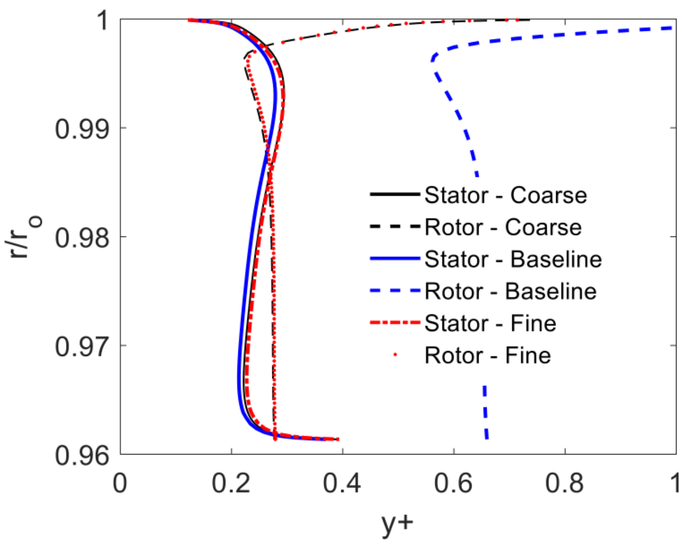

Figure 12. y^+ at one grid point away from the stator and rotor walls around the seal for the three grids used—coarse, baseline, and fine.

On the time step size, it needs to be small enough to resolve the small time scales in the flow. The Kolmogorov time scale, $\tau_\eta = (\nu/\varepsilon)^{0.5}$, can be used as a starting point to estimate the necessary time step size. Figure 13 shows the Kolmogorov time scale, τ_η, obtained from the RANS solution based on the SST model. From Figure 13, the time scale that needs to be resolved is between 10^{-7} and 10^{-5} s. A time step-size sensitivity study showed that $\Delta t = 10^{-6}$ s is adequate.

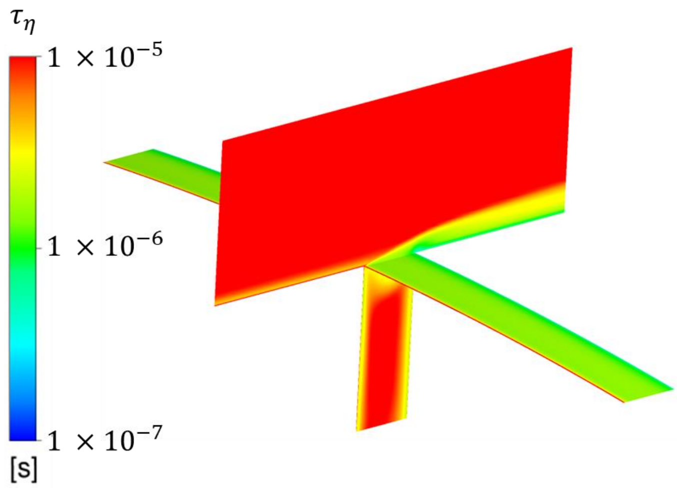

Figure 13. Kolmogorov time scale, τ_η, around the seal.

The results of the grid sensitivity for $\Delta t = 10^{-6}$ are given in Figures 14 and 15. These two figures show the circumferentially averaged mean (time-averaged) azimuthal and radial velocities as a function of z in the seal at three radial locations—r = 0.966 $r_o = 112.25$ mm, $r = 0.983\ r_o = 114.25$ mm, and $r = 0.991\ r_o = 115.25$ mm—obtained by using the three grids shown in Figure 11. Also shown in those figures are the experimental data from Bohn et al. [12]. From Figures 14 and 15, RANS can be seen to give the highest azimuthal velocity in the seal, whereas LES gives the lowest azimuthal velocity in the seal. This is because LES predicts higher turbulent mixing than RANS. For azimuthal velocities, LES results match the experimental data better than RANS. For radial velocities, RANS generally gives lower magnitudes between the disks, whereas LES generally gives higher magnitudes. In this case, RANS matches well with the experimental data. The LES profiles for the azimuthal and radial velocities obtained in this study are similar to those obtained in the LES study reported by Gao et al. [17] with a 13.33-degree sector. The reason for discrepancies between the LES results and the experimental data is discussed in the next sub-section.

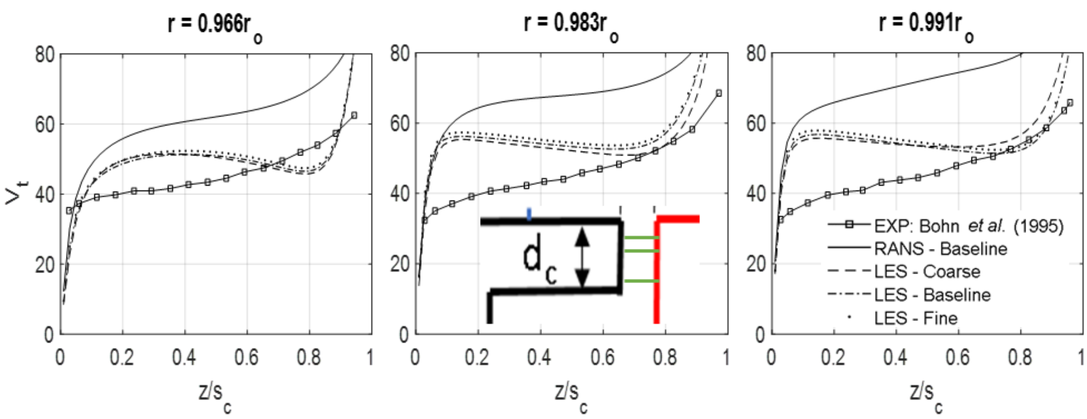

Figure 14. Mean azimuthal velocities in the seal clearance [12].

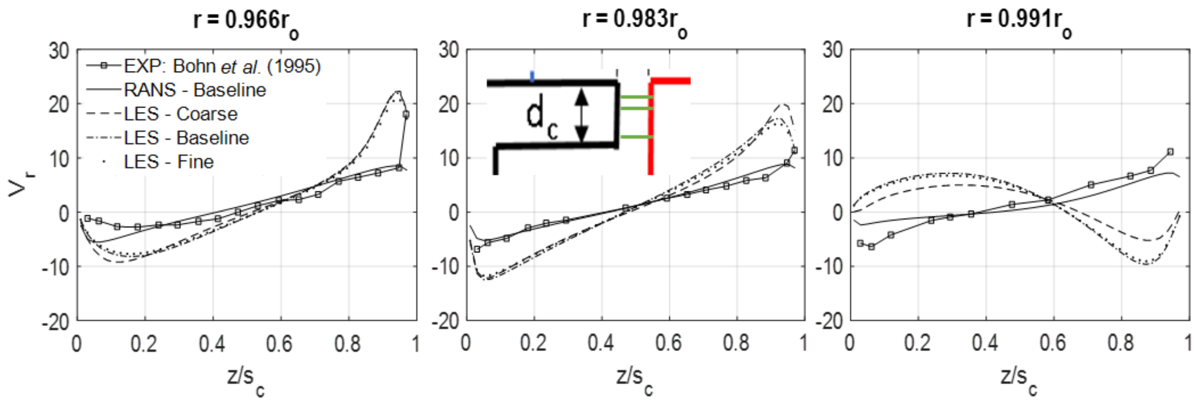

Figure 15. Mean radial velocities in the seal clearance [12].

Figure 16 shows the energy spectra based on the radial velocities from five probes in the seal region for the baseline grid. From this figure, it can be seen that the energy spectra follow Kolmogorov's $-5/3$ law for a range of frequencies before falling. The energy densities associated with high frequencies are at least seven orders lower than the energy densities corresponding to low frequencies in the inertial sub-range. Therefore, the grid resolution (baseline grid) is adequate for the rim seal configuration.

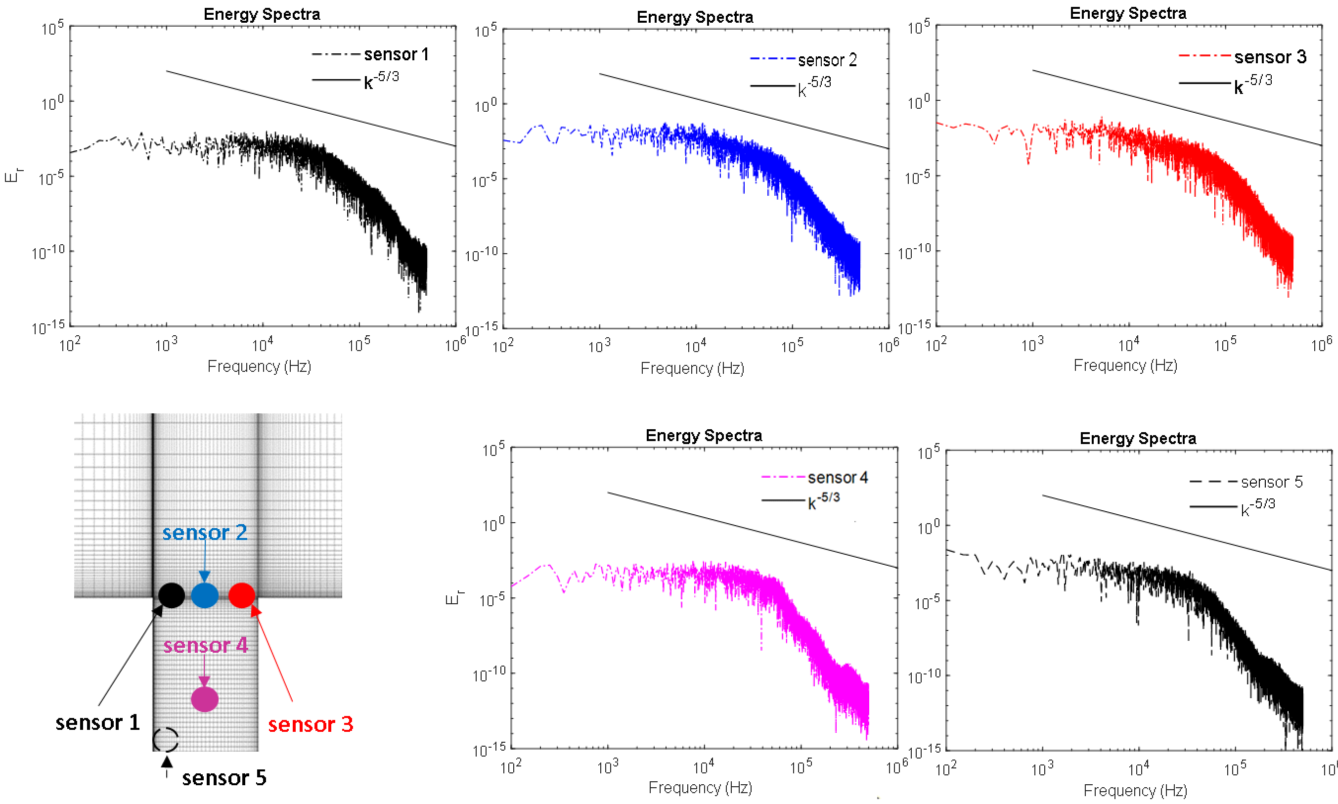

Figure 16. Energy spectra at five points in the seal.

5.1.3. Effects of Inlet Turbulence and Velocity Profile on Flow in Seal

Regarding validation, the most challenging part is to ensure that the computational study is solving the same problem as the experimental study. For the rotor–stator configuration studied, the thickness of the boundary layer at an upstream location where the flow is still unaffected by the seal and rotor should be provided by the experimental study, but it was not. Thus, this computational study assumed "fully-developed" turbulent flow in the annulus of the hot gas path with $I = 3\%$ at the inflow boundary, and the resulting comparisons are given in Figures 14 and 15. To examine the effects of boundary-layer thickness, an LES was performed using a fully developed turbulent profile and $I = 0$ at the inflow boundary (i.e., the LES has no turbulent fluctuations). Without turbulent fluctuations, the fully developed profile could not be sustained by LES, and the velocity profile approaches that of a laminar profile because shear is only driven by viscosity.

Figure 17 shows the effects of the velocity and turbulent intensity imposed at the inflow boundary on the mean azimuthal and radial velocities in the seal clearance. From this figure, those effects can be seen to be quite large, which explains the significant difference between the experimental and LES results given in Figures 14 and 15. Thus, experimental and computational studies must characterize the flow upstream of the seal in their studies. In this study, all results presented from this point onward have a "fully-developed" turbulent flow approaching the seal. Figures 18 and 19 show the effects of inlet turbulence, I, on the number of frequency modes and the number and size of flow structures via pressure in the seal. From Figure 18, inlet turbulence can be seen to increase the number of dominant modes (frequencies). From Figure 19, inlet turbulence can be seen to break up large vortical structures into many smaller structures.

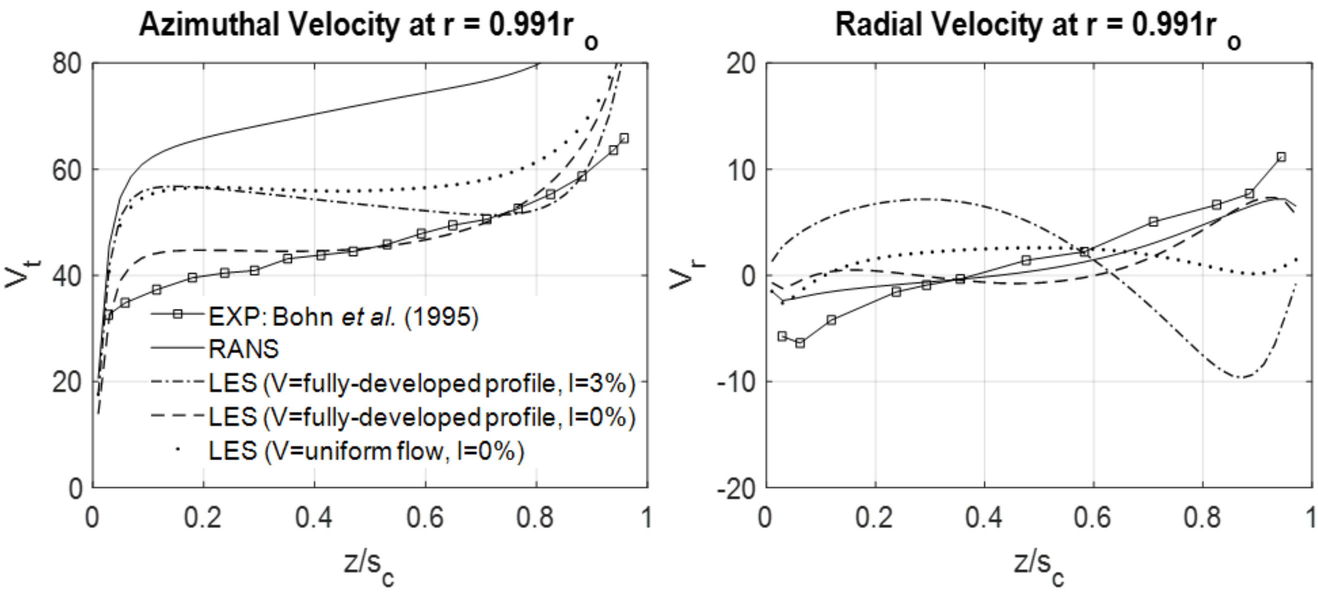

Figure 17. Effects of inflow boundary conditions on azimuthal and radial velocities in the seal [12].

5.2. Flow Field Induced by Rotor and Its Rotation

The flow field induced by the rotor and its rotation on ingress and egress is described in three parts: the instantaneous flow, the time-averaged flow, and the trajectory of the mean flow connected to the ingress and egress.

5.2.1. Instantaneous Flow Field

The instantaneous flow from LES with I = 3% at the inflow boundary is given in Figures 19–25. Figures 19–24 show the instantaneous pressure, vorticity, and velocity, and Figure 25 shows power spectral density (PSD) for pressure at several locations around the seal. From Figures 20–22, one can see the shedding of vortices at the seals' backward-facing step and their impingement at the seal's forward-facing step via the vorticity and pressure contours. Figure 22 also shows a wavy shear layer in the azimuthal direction around the rotor surface at r = r_o via alternating regions of high and low velocity magnitudes. This wavy shear layer with its corresponding wavy displacement thickness, is created by two mechanisms: (1) Kelvin–Helmholtz instabilities (KHI) that form from the interaction between the hot gas flow in the axial direction and the boundary-layer flow in the azimuthal direction above the rotating rotor, and (2) vortex shedding (VS) on the backward-facing step of the seal. This wavy displacement thickness causes alternating region of high and low pressures on the rotor side of the seal, and this can be seen in Figures 19, 23 and 24. At $z = -10^{-3}$ mm, Figures 19 and 24 show the pressure peaks and vortical structures repeating six to seven times over a 10-degree sector so that the frequency, f, normalized by the frequency of the rotor's rotation, f_ω, is $f/f_\omega = 6 \times 36 = 216$ to $7 \times 36 = 252$.

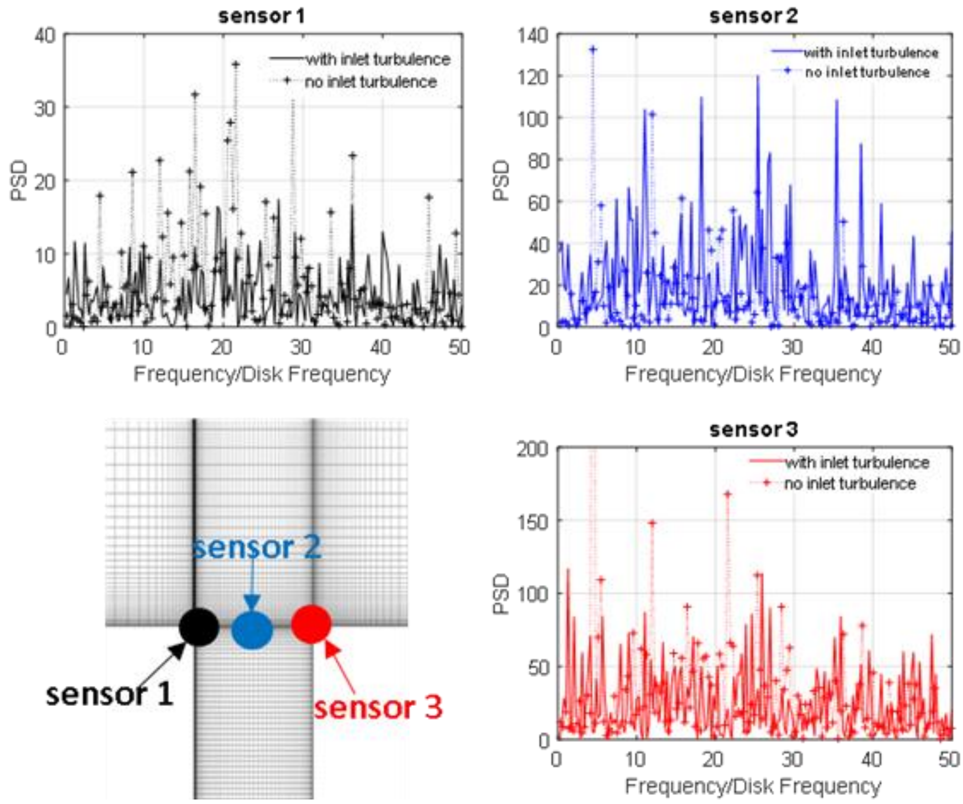

Figure 18. Effects of turbulent intensity (*I*) at the inflow boundary on the power spectral density (PSD) of pressure at three locations.

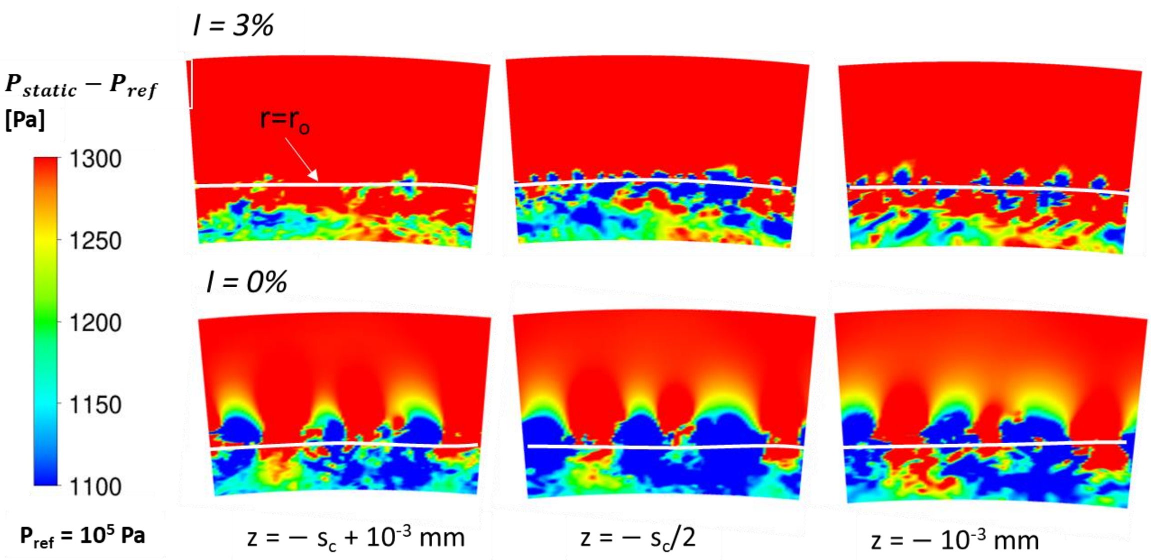

Figure 19. Effects of turbulent intensity (*I*) at the inflow boundary on the instantaneous pressure around the seal.

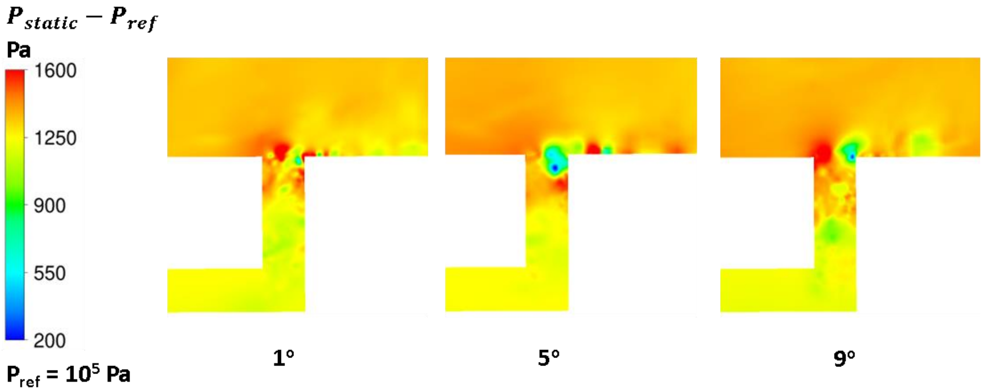

Figure 20. Instantaneous pressure in three r–z planes (c_W = 1000).

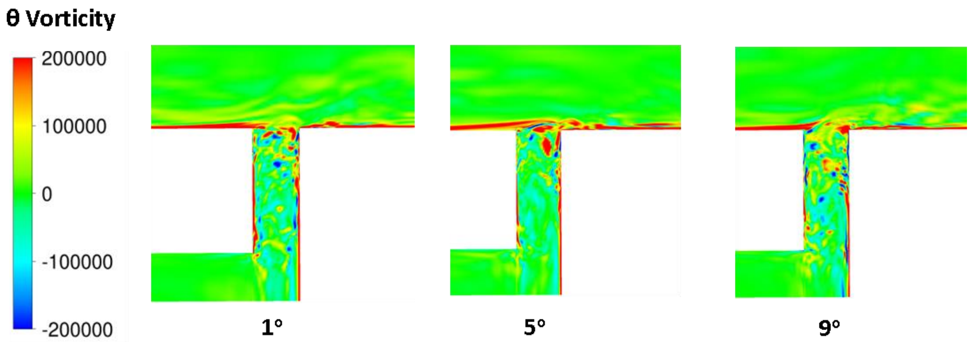

Figure 21. Instantaneous vorticity magnitude in three r–z planes (c_W = 1000).

From sensor 3 in Figure 25, the fluctuating energy in the pressure associated with the vortical structures and pressure streaks that peak at $f/f_\omega = 216$ to 252 can be seen to be quite low, indicating that those structures are essentially stationary. Additionally, time-averaging shows that they do not rotate in the azimuthal direction with the rotor. Data from this sensor also show the energy associated with the unsteadiness connected to the large scales of the KHI, VS, and turbulence to have many dominant frequencies. By not being dominated by a single frequency, the frequencies observed are not triggered by acoustics from the geometry [28]. At sensors 4 and 5, the PSD of the fluctuations are considerably lower with fewer peaks because KHI and VS do not affect this region.

5.2.2. Time-Averaged Flow Field

Figures 26–30 show the time-averaged mean pressure, temperature, and velocity obtained by LES and RANS for the rotor–stator configuration studied with and without sealing flow. From Figure 26, one can see that there are alternating regions of high and low pressure around the rotor surface. This is created by impingement of the hot gas flow on the wavy displacement thickness produced by the KHI and VS described in the previous subsection. Figure 26 also shows the alternating regions of high and low pressure to be nearly equally spaced. The number of streaks is 12 over a 10-degree sector, which corresponds to a normalized frequency of $f/f_\omega = 12 \times 36 = 432$, and this is twice the normalized frequency of the wavy shear layer created by the KHI and VS. From Figures 26 and 27, the difference between the high and low pressures can be seen to be less if there is no sealing flow. This because without sealing flow, the ingress into the seal is higher, which removes more of the lower momentum air next to the stator surface at r = r_o, and this reduces the boundary-layer thickness and hence the displacement thickness on the rotor side of the seal. With a thinner displacement thickness, the stagnation region due to impingement is reduced. Though Figure 26 shows the number of streaks in pressure predicted by LES and RANS to be the same, Figures 27 and 28 show that the pressure distribution within the seal predicted by LES to be very different from those predicted by

RANS. Because of this difference in pressure in and around the seal, RANS was unable to predict ingress. Figure 29 shows how LES predicts very different temperature distributions in the seal and wheelspace when compared with RANS. The reason is that LES could predict the ingress of hot gas into the seal and wheelspace, whereas RANS could not.

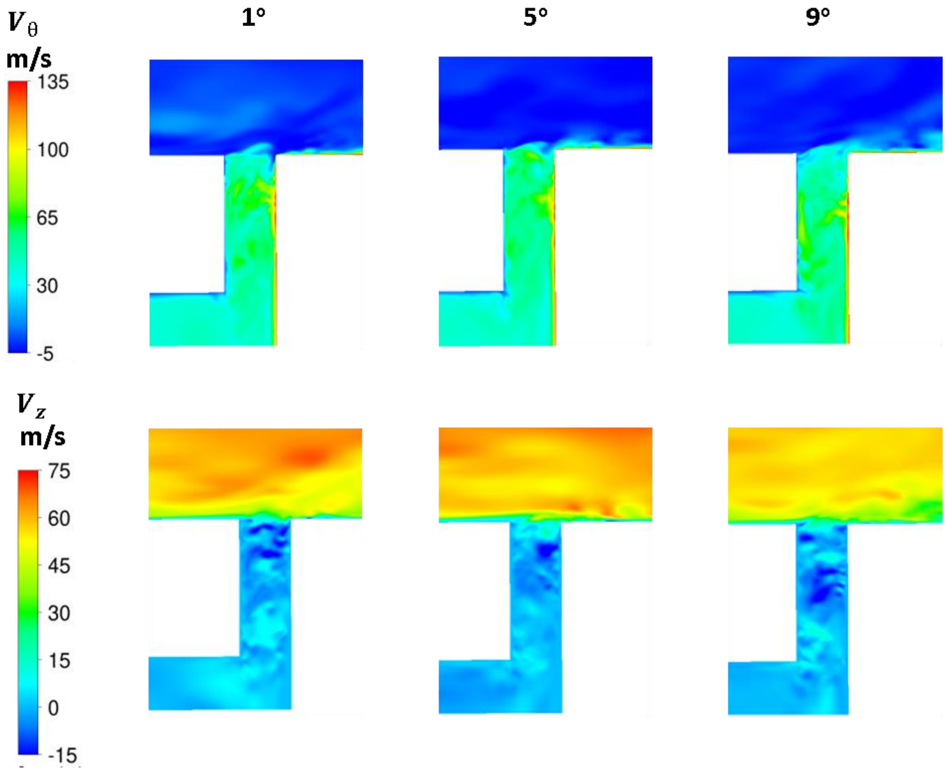

Figure 22. Instantaneous azimuthal and axial velocity magnitudes in three r–z planes (c_W = 1000).

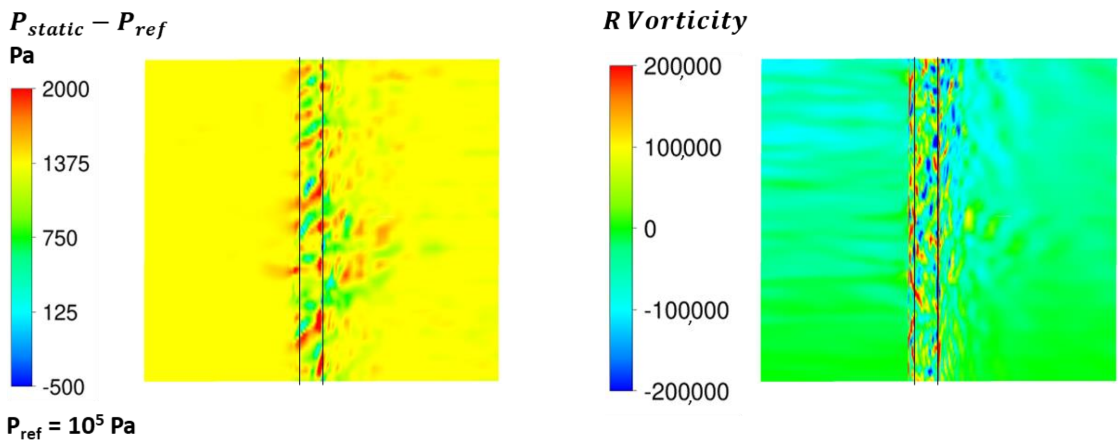

Figure 23. Instantaneous pressure and radial-vorticity magnitude at r = r_o (c_W = 1000).

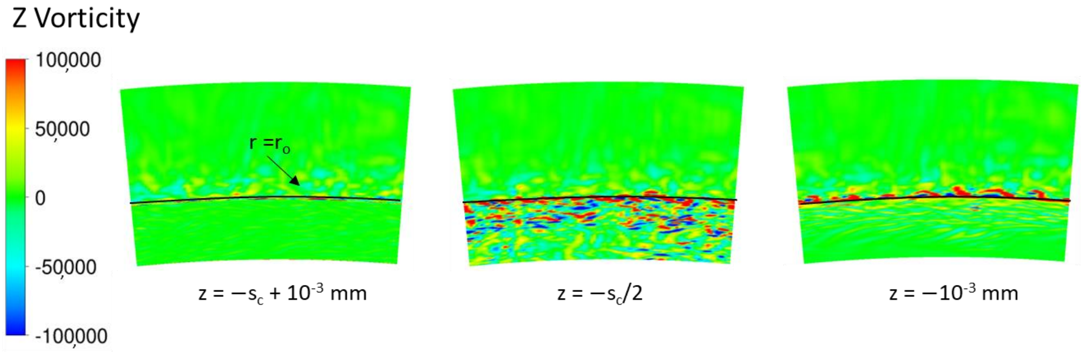

Figure 24. Instantaneous magnitude of the vorticity in the axial direction at three r–θ planes around the seal (c_W = 1000).

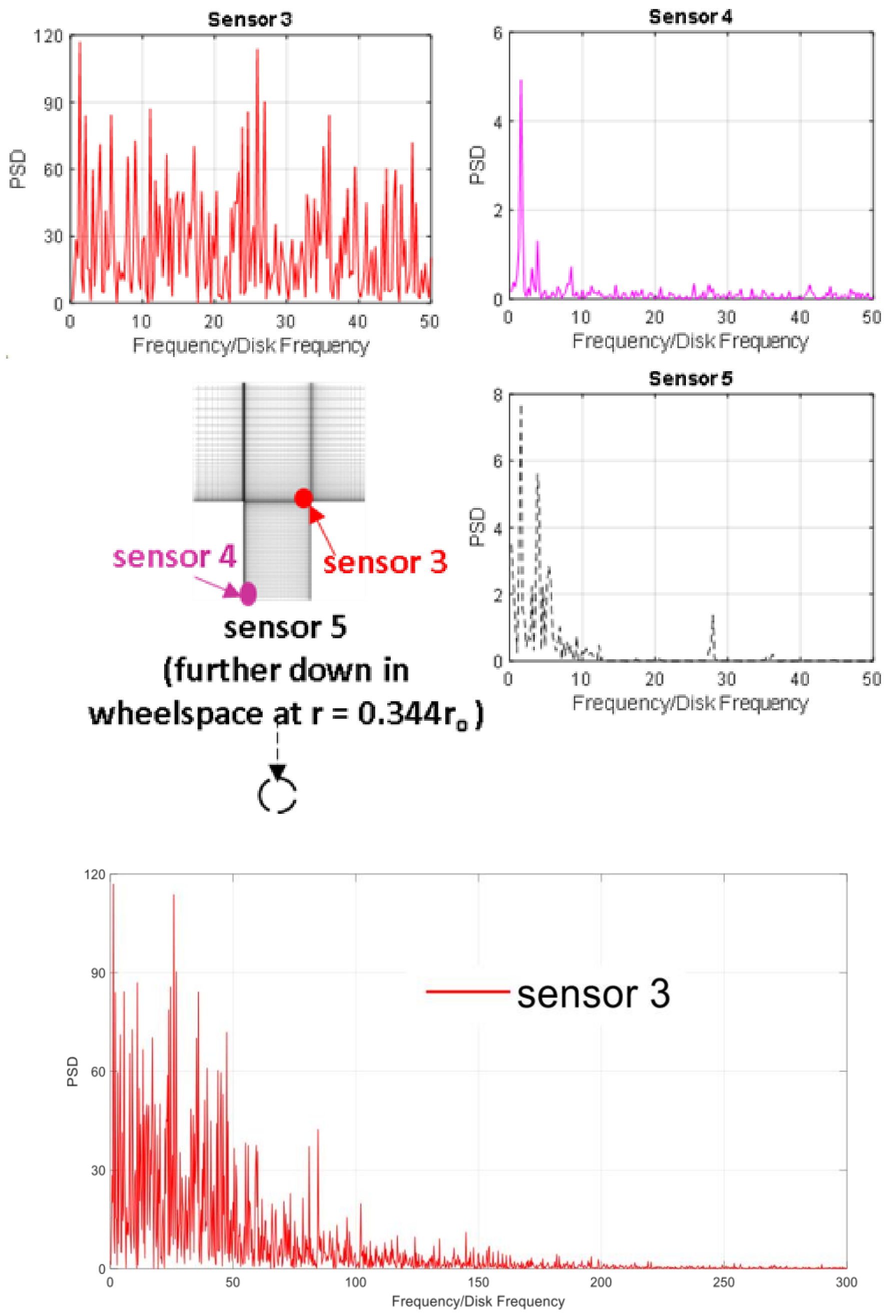

Figure 25. Power spectral density (PSD) of pressure at three sensor locations (c_W = 1000).

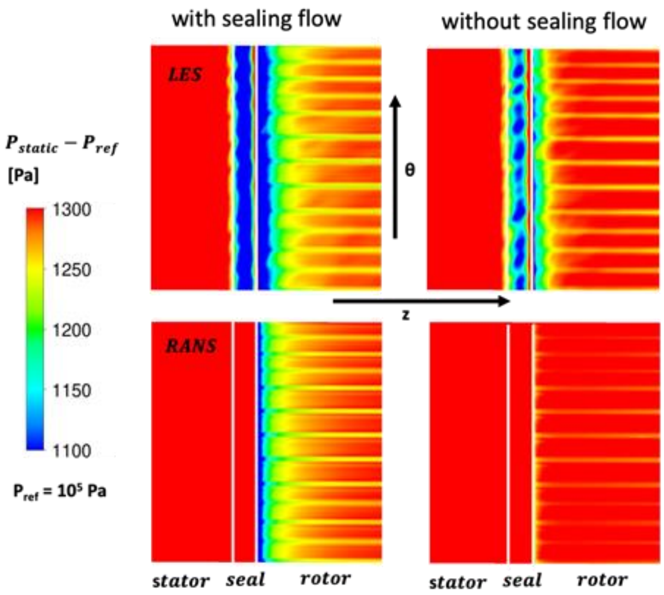

Figure 26. Mean pressure from LES and RANS on the surface of the stator and rotor at r = r_o with and without sealing flow.

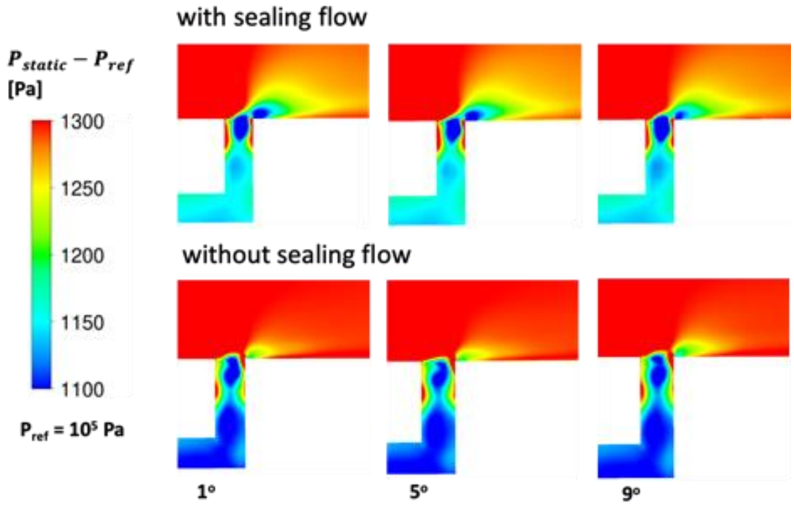

Figure 27. Mean pressure from LES in three r–z planes with and without sealing flow.

Figure 30 shows the time-averaged velocity projected in an r–z plane at θ = 5° around the seal. From this figure, the hot gas flow can be seen to separate at the backward-facing step of the seal on the stator disk. Since the seal's length-to-the-clearance ratio (d_c/s_c = 4.5/1.7 = 2.6) is appreciable, this separated flow driven by the hot gas flow over the seal can be seen to generate a series of recirculating flows within the seal. These recirculating flows affect ingress and egress, and this is described in the next subsection. One reason why RANS could not predict ingress is because the RANS solution based on SST cannot account for the effects of small-scale turbulent structures, shown schematically in Figure 31, that could become entrained into the seal and thereby affect the nature of the recirculating flows around the seal.

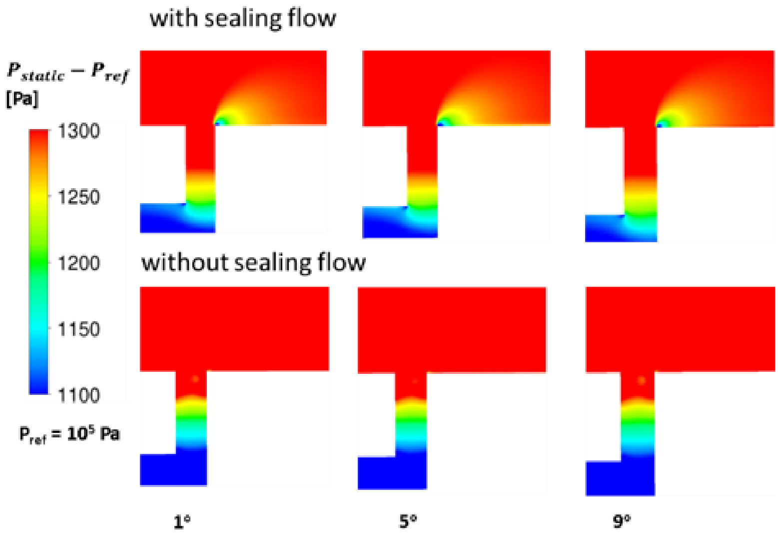

Figure 28. Mean pressure from RANS in three r–z planes with and without sealing flow.

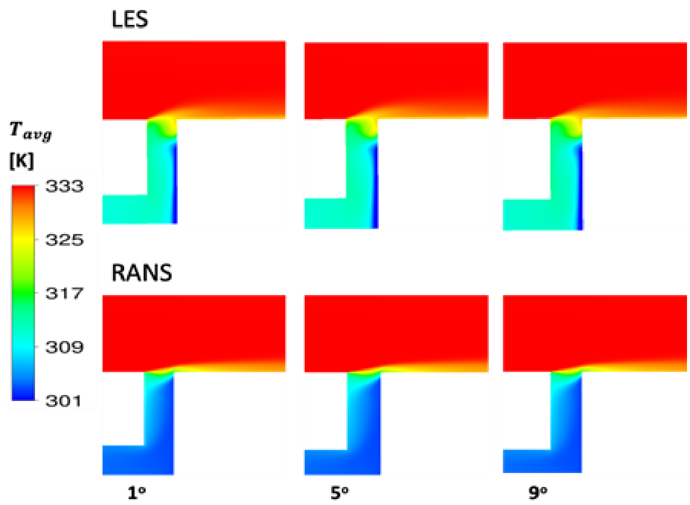

Figure 29. Mean temperature from LES and RANS in three r–z planes with sealing flow.

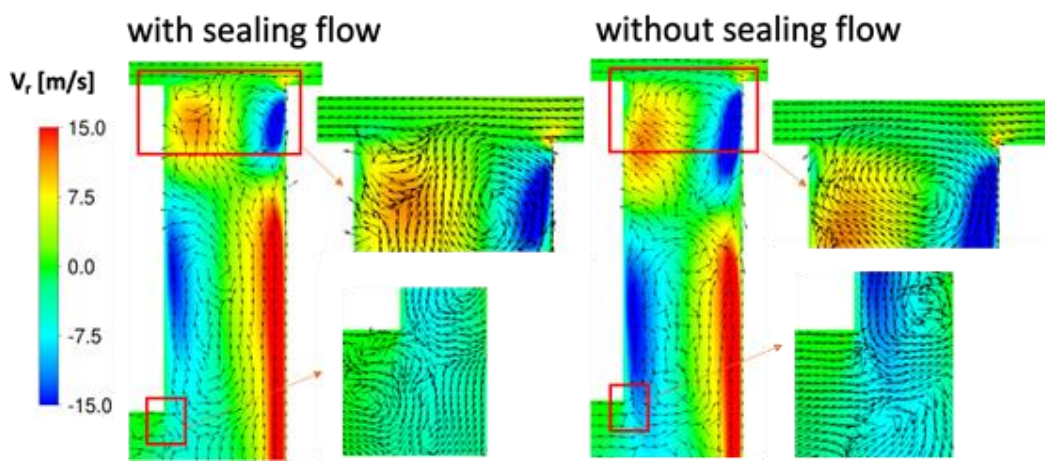

Figure 30. Mean velocity projected in an r–z plane at θ = 5° colored by magnitude of the radial velocity with and without sealing flow from LES.

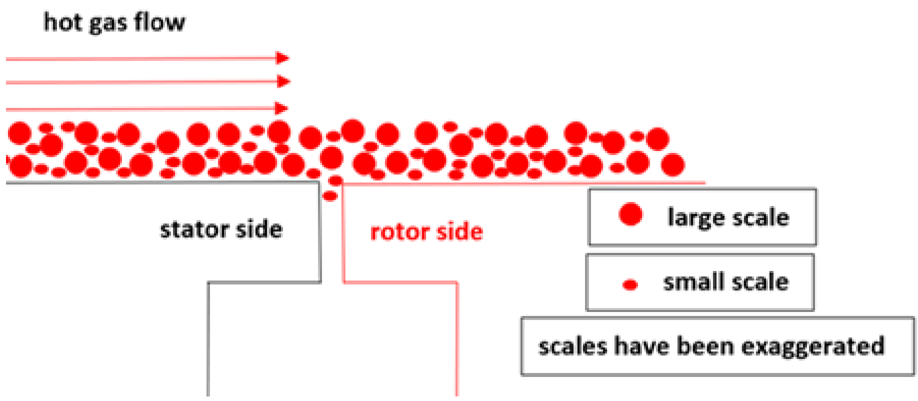

Figure 31. Schematic of eddy sizes in the turbulent flow around the seal (not drawn to scale).

5.2.3. Mean Trajectories of Ingress and Egress

For the rotor–stator configuration examined in this study with no vanes and blades, ingress and egress are only affected by the flow rate of the hot gas, the rotor and its rotational speed, the sealing flow rate, and the geometry of the seal. The complex flow field created by the interactions among these parameters are summarized in the previous section. As noted, interactions between the hot gas flow in the axial direction and the boundary-layer flow in the azimuthal direction created by the rotor's rotation causes KHI to occur just downstream of the seal. The recirculating flow in the seal clearance, driven by the hot gas flow over the seal, spirals because of the rotor's rotation and undulates because of VS at the backward-facing side of the seal. Since the magnitude of the azimuthal velocity in the seal is much higher than its axial velocity, the spiraling flow travels a significant distance along the azimuthal direction before completing one revolution of the recirculating flow. This can be seen in Figure 32, which shows trajectories that originate from the hot gas and from the sealing flow. Detailed analysis of these trajectories and the pressure field around them shows that ingress occurs on the rotor side, where regions with high pressure deflect fluid particles into adjacent regions with lower pressure. Once entering into the seal clearance, it is entrained by shed vortices and the spiraling recirculating flow.

Depending on the momentum imparted to the ingested flow by the alternating regions of high and low pressure in the azimuthal direction, the ingested flow could exit the seal or become entrained by another spiraling recirculating flow deeper in the seal and eventually entering into the wheelspace. Figure 33 shows a schematic of the three possible trajectories of the hot gas flow when approaching the seal. The first is flowing past the seal (i.e., never enters the seal; thus, no ingress). The second is flowing into the seal but spirals back out. For this case, the ingress only heats the material in the seal region. The third is flowing into seal and eventually into the wheelspace. For this case, the ingressed hot gas heats the stator and rotor disks and thus is problematic.

For the configuration studied, all sealing flows must exit the seal (i.e., egress). The trajectory is depicted in Figure 34. The sealing flow travels along the rotor disk in a spiraling fashion as shown in Figure 32 until reaching the recirculating flow in the seal. This recirculating flow entrains the sealing flow towards the stator disk. The sealing flow then exits the seal from the stator side of the seal.

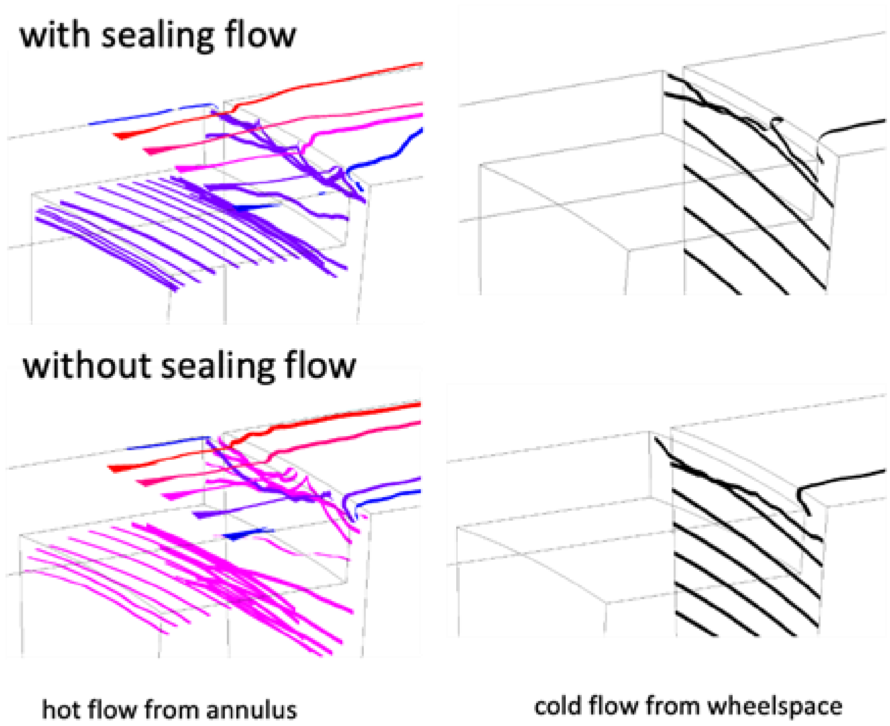

Figure 32. Ingress from hot gas flow (**left**) and egress from sealing flow (**right**) with and without sealing flow based on mean flow from LES. Different colors represent different flow trajectories.

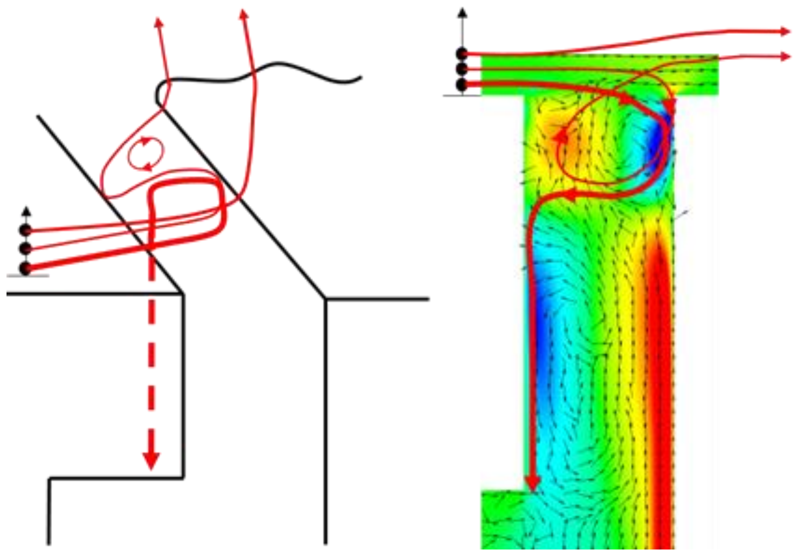

Figure 33. Schematic of hot gas flow trajectory into the wheelspace through the seal (ingress) and into and out of seal (egress) based on mean flow from LES.

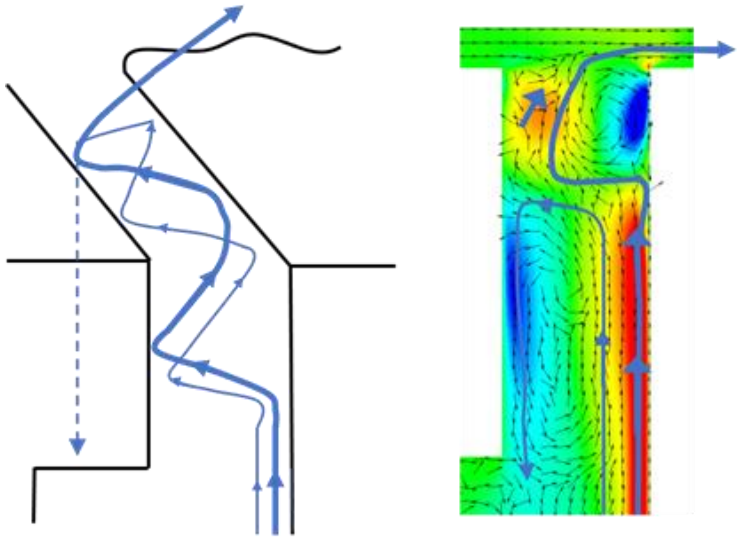

Figure 34. Schematic of sealing flow trajectory exiting the wheelspace through the seal (egress) based on mean flow from LES.

6. Summary and Conclusions

Ingress and egress through rim seals are driven by (1) the rotor and its rotation, (2) the pressure variation around the stator vanes' trailing edges, and (3) the stagnation pressures induced by the rotor disk and its blades. In this study, large eddy simulations were performed to examine rotationally induced ingress in a rotor–stator configuration without vanes and blades. Key findings are as follows:

- Interaction between the hot gas flow in the axial direction and the boundary-layer flow in the azimuthal direction induced by the rotating rotor causes Kelvin–Helmholtz instability (KHI) to occur.
- The KHI forms a wavy boundary layer in the azimuthal direction with a corresponding wavy displacement thickness.
- Hot gas flow over the seal induces a series of recirculating flows in the seal clearance and causes vortex shedding at the seal's backward-facing step.
- The wavy displacement thickness formed by KHI and the impingement of shed vortices on the rotor side of the seal create alternating regions of high and low pressures around the rotor side of the seal.
- The alternating regions of high and low pressures cause ingress to start on the rotor side of the seal.
- Regions of high and low pressures around the rotor side of the seal were found to be statistically stationary and do not rotate with the rotor.
- Not all hot gases ingested into the seal reach the wheelspace because the motion induced by the spiraling recirculating flow entrains them back out into the hot gas path.
- On egress, it starts on the rotor side because of "disk pumping" in the wheelspace. However, once reaching the clearance of the seal, it becomes entrained by the recirculating flows there and exits from the stator side.
- Though RANS with the SST model was able to predict regions of high and low pressures around the rotor side of the seal, it was unable to predict ingress. LES coupled with the WALE model could predict regions of high and low pressures around the rotor side of the seal and the ingress that they create.

This study isolated the effects of rotationally induced ingress, which dominates when $Re_w/Re_\phi \ll 1$. To minimize rotationally induced ingress, the seal geometry should be designed to weaken features that create and magnify the strength of the alternating regions of high and low pressures. Additionally, the recirculating flow in the seal clearance should be modified to minimize the entrainment of the hot gas into the seal.

Author Contributions: Conceptualization, S.N. and T.I-P.S.; Methodology, S.N. and T.I-P.S.; validation, S.N.; formal analysis, S.N. and T.I-P.S.; writing—original draft preparation, S.N. and T.I-P.S.; writing—review and editing, S.N., T.I-P.S., K.B., R.D. and R.A.D.; funding acquisition, K.B., R.D. and R.A.D. All authors have read and agreed to the published version of the manuscript.

Funding: This project was supported by the Ames National Laboratory and the National Energy Technology Laboratory of the U.S. Department of Energy under Contract No. DE-AC02-07CH11358/Agreement No. 26110-AMES-CMI. The authors are grateful for this support.

Conflicts of Interest: The authors declare no conflict of interest.

Nomenclature

c_W	nondimensional coolant flow rate: $c_W = \dot{m}_c/\mu_c r_o$
D_h	hydraulic diameter
G	gap ratio
G_c	clearance ratio
H	height of annulus (see Figures 3 and 4)
I	turbulence intensity
L_i	length (i = 1, 2, 3, 4, 5; see Figures 3 and 4)
$\dot{m}$	mass flow rate
P	pressure
P_b	back pressure
r	radial coordinate
r_o	radius of hub/inner radius of annulus
r_1	outer radius of annulus
Re_{D_h}	Reynolds number in a duct: $Re_{D_h} = \rho_h U_b D_h/\mu$
Re_w	external flow Reynolds number: $Re_w = \rho_h V_h r_o/\mu_h$
Re_ϕ	rotational Reynolds number: $Re_\phi = \rho_h \omega r_o^2/\mu_h$
s	axial distance between rotor and stator (gap)
s_c	axial distance in seal opening (clearance)
T	temperature
$\widetilde{u}$	rms of tangential velocity fluctuation in annular duct
U	time-average axial velocity in annular duct
U_b	average bulk velocity magnitude in a duct
u_τ	friction velocity: $u_\tau = \sqrt{\tau_w/\rho}$, where τ_w is the "local" wall shear stress
$\widetilde{v}$	rms of radial velocity fluctuation in annular duct
$\overline{vw}$	axial-radial-velocity cross-correlation
V	velocity
$\widetilde{w}$	rms of axial velocity fluctuation in annular duct
y^+	nondimensional turbulent distance
z	axial coordinate
γ	curvature parameter: $\gamma = r_1 - r_o/2r_o$
δ	boundary layer thickness
ε	rate of turbulence dissipation
θ	azimuthal coordinate
μ	dynamic viscosity
ν	kinematic viscosity
$\nu_{t,eff}$	effective turbulent kinematic viscosity
ρ	density
τ_η	Kolmogorov time scale: $\tau_\eta = (\nu/\varepsilon)^{0.5}$
$\Delta\phi^+$	normalized grid spacing: $\Delta\phi^+ = \Delta\phi u_\tau/\nu$ where $\Delta\phi = \Delta r,\ \Delta z,\ r\Delta\theta$
ω	angular speed of rotor disk
Subscripts	
c	coolant flow
h	mainstream flow

References

1. Han, J.-C. Advanced Cooling in Gas Turbines 2016 Max Jakob Memorial Award Paper. ASME. *J. Heat Transf.* **2018**, *140*, 113001. [CrossRef]
2. Goldstein, R.J.; Chen, H.P. Film Cooling on a Gas Turbine Blade Near the End Wall. *J. Eng. Gas Turbines Power* **1985**, *107*, 117–122. [CrossRef]
3. Tin, S.; Pollock, T.M. Nickel-Base Superalloys in Advanced Turbine Engines. In *Turbine Aerodynamics, Heat Transfer, Materials, and Mechanics*; Shih, T.I.-P., Yang, V., Eds.; AIAA Progress Series; American Institute of Aeronautics and Astronautics: Washington, DC, USA, 2014; Volume 243.
4. Choi, S.; Choi, S.; Cho, H. Effect of Various Coolant Mass Flow Rates on Sealing Effectiveness of Turbine Blade Rim Seal at First Stage Gas Turbine Experimental Facility. *Energies* **2020**, *13*, 4105. [CrossRef]
5. Owen, J.M.; Phadke, U.P. An Investigation of Ingress for a Simple Shrouded Rotating Disc System with a Radial Outflow of Coolant. In Proceedings of the ASME 1980 International Gas Turbine Conference and Products Show, New Orleans, LA, USA, 10–13 March 1980; Volume 1A: General. [CrossRef]
6. Phadke, U.P.; Owen, J.M. An Investigation of Ingress for an "Air-Cooled" Shrouded Rotating Disk System with Radial-Clearance Seals. *J. Eng. Power* **1983**, *105*, 178–182. [CrossRef]
7. Phadke, U.P.; Owen, J.M. Aerodynamic Aspects of the Sealing of Gas-Turbine Rotor-Stator Systems. Part 1: The Behavior of Simple Shrouded Rotating-Disk Systems in a Quiescent Environment. *Int. J. Heat Fluid Flow* **1988**, *9*, 98–105. [CrossRef]
8. Phadke, U.P.; Owen, J.M. Aerodynamic Aspects of the Sealing of Gas-Turbine Rotor-Stator Systems. Part 2: The Performance of Simple Seals in a Quasi-Axisymmetric External Flow. *Int. J. Heat Fluid Flow* **1988**, *9*, 106–112. [CrossRef]
9. Phadke, U.P.; Owen, J.M. Aerodynamic Aspects of the Sealing of Gas-Turbine Rotor-Stator Systems. Part 3: The Effect of Nonaxisymmetric External Flow on Seal Performance. *Int. J. Heat Fluid Flow* **1988**, *9*, 113–117. [CrossRef]
10. Sangan, C.M.; Pountney, O.J.; Zhou, K.; Owen, J.M.; Wilson, M.; Lock, G.D. Experimental Measurements of Ingestion Through Turbine Rim Seals—Part II: Rotationally Induced Ingress. *J. Turbomach.* **2013**, *135*, 021013. [CrossRef]
11. Dadkhah, S.; Turner, A.B.; Chew, J.W. Performance of Radial Clearance Rim Seals in Upstream and Downstream Rotor–Stator Wheelspaces. *J. Turbomach.* **1992**, *114*, 439–445. [CrossRef]
12. Bohn, D.; Johann, E.; Krüger, U. Experimental and Numerical Investigations of Aerodynamic Aspects of Hot Gas Ingestion in Rotor-Stator Systems with Superimposed Cooling Mass Flow. In Proceedings of the ASME 1995 International Gas Turbine and Aeroengine Congress and Exposition, Houston, TX, USA, 5 June 1995; Volume 1: Turbomachinery. [CrossRef]
13. Cao, C.; Chew, J.W.; Millington, P.R.; Hogg, S.I. Interaction of Rim Seal and Annulus Flows in an Axial Flow Turbine. *J. Eng. Gas Turbines Power* **2004**, *126*, 786–793. [CrossRef]
14. Boudet, J.; Autef, V.; Chew, J.; Hills, N.; Gentilhomme, O. Numerical Simulation of Rim Seal Flows in Axial Turbines. *Aeronaut. J.* **2005**, *109*, 373–383. [CrossRef]
15. Jakoby, R.; Zierer, T.; Lindblad, K.; Larsson, J.; deVito, L.; Bohn, D.; Funcke, J.; Decker, A. Numerical Simulation of the Unsteady Flow Field in an Axial Gas Turbine Rim Seal Configuration. In Proceedings of the ASME Turbo Expo 2004: Power for Land, Sea, and Air, Vienna, Austria, 14–17 June 2004; Volume 4: Turbo Expo 2004, pp. 431–440. [CrossRef]
16. Rabs, M.; Benra, F.-K.; Dohmen, H.J.; Schneider, O. Investigation of Flow Instabilities Near the Rim Cavity of a 1.5 Stage Gas Turbine. In Proceedings of the ASME Turbo Expo 2009: Power for Land, Sea, and Air, Orlando, FL, USA, 8–12 June 2009; Volume 3: Heat Transfer, Parts A and B, pp. 1263–1272. [CrossRef]
17. Gao, F.; Chew, J.; Beard, P.; Amirante, D.; Hills, N. Large-Eddy Simulation of Unsteady Turbine Rim Sealing Flows. *Int. J. Heat Fluid Flow* **2018**, *70*, 160–170. [CrossRef]
18. Liu, J.; Weaver, A.; Shih, T.I.-P.; Sangan, C.M.; Lock, G.D. Modelling and Simulation of Ingress into the Rim Seal and Wheelspace of a Gas-Turbine Rotor-Stator Configuration. In Proceedings of the 53rd AIAA Aerospace Sciences Meeting, Kissimmee, FL, USA, 5–9 January 2015. [CrossRef]
19. Menter, F.R. Zonal Two-Equation k-ω Turbulence Models for Aerodynamic Flows. In Proceedings of the 23rd Fluid Dynamics, Plasmadynamics, and Lasers Conference, Orlando, FL, USA, 6–9 July 1993.
20. Nicoud, F.; Ducros, F. Subgrid-Scale Stress Modelling Based on the Square of the Velocity Gradient Tensor. *Flow Turbul. Combust.* **1999**, *62*, 183–200. [CrossRef]
21. Dhamankar, N.; Blaisdell, G.; Lyrintzis, A. Overview of Turbulent Inflow Boundary Conditions for Large-Eddy Simulations. *AIAA J.* **2018**, *56*, 1317–1334. [CrossRef]
22. Available online: https://www.ansys.com/products/fluids/ansys-fluent (accessed on 22 May 2023).
23. Patankar, S.V. *Numerical Heat Transfer and Fluid Flow*; Hemisphere Publishing Corp.: Washington, DC, USA, 1980.
24. Nouri, J.; Umur, H.; Whitelaw, J. Flow of Newtonian and non-Newtonian Fluids in Concentric and Eccentric Annuli. *J. Fluid Mech.* **1993**, *253*, 617–641. [CrossRef]
25. Quadrio, M.; Luchini, P. Direct Numerical Simulation of the Turbulent Flow in a Pipe with Annular Cross-section. *Eur. J. Mech. B/Fluids* **2002**, *21*, 413–427. [CrossRef]
26. Kim, J.; Moin, P.; Moser, R. Turbulence Statistics in Fully Developed Channel Flow at Low Reynolds Number. *J. Fluid Mech.* **1987**, *177*, 133–166. [CrossRef]

27. Celik, I.B.; Cehreli, Z.N.; Yavuz, I. Index of Resolution Quality for Large Eddy Simulations. *J. Fluids Eng.* **2005**, *127*, 949–958. [CrossRef]
28. Schädler, R.; Kalfas, A.I.; Abhari, R.S.; Schmid, G.; Voelker, S. Modulation and Radial Migration of Turbine Hub Cavity Modes by the Rim Seal Purge Flow. *J. Turbomach.* **2017**, *139*, 011011. [CrossRef]